

# LUNAR REFLECTANCE MODELING FOR TERRAIN RELATIVE NAVIGATION

Carl De Vries\* and John Christian†

Feature matching techniques often encode a brightness pattern from an image without knowledge of the underlying scene. This makes feature matching difficult when illumination conditions change significantly between images or are not consistent with onboard maps. The brightness patterns in images of the lunar surface can be partially described by a surface reflectance model which can often be parameterized by quantities known onboard from a sun sensor and calibrated camera. Unfortunately, these models can be intractable due to their complexity. This work develops a reduced-order lunar reflectance model for future illumination-informed feature descriptor development.

## INTRODUCTION

The commitment of space agencies and commercial resources to lunar and small-body exploration in recent years is expected to continue growing for the foreseeable future. One of the primary technical challenges is performing autonomous, precision landing to reach locations of scientific value. When a spacecraft is near the surface of a body, navigation states may be estimated from optical measurements of natural surface landmarks. Now, it's well-known that the appearance of a scene is influenced by the illumination and viewing conditions under which the image is captured.<sup>1,2</sup> When changes in scene illumination are large, feature matching becomes a difficult challenge for vision-based terrain relative navigation (TRN, e.g. cameras) systems. This work explores the development of a reduced-order lunar reflectance model for illumination-informed feature matching.

Under consistent illumination and viewing conditions, several effective vision-based TRN techniques are available to spacecraft navigators.<sup>3</sup> When onboard reference maps are unavailable, visual odometry (VO) techniques may be used to estimate a spacecraft's motion as demonstrated by the Descent Image Motion Estimation System (DIMES) on the Mars Exploration Rovers (MERs).<sup>4</sup> When an onboard map is available, then image features may be matched against a curated set of cataloged features as demonstrated by Mars Perseverance's Lander Vision System (LVS)<sup>5</sup> and OSIRIS-REx's Natural Feature Tracking (NFT).<sup>6</sup> Regardless of the TRN architecture, feature matching is a common, non-trivial task.

In many cases, it's possible to match features by encoding the intensity pattern surrounding a feature into a descriptor. One approach, template matching, has a well-established history in space-flight applications,<sup>4-6</sup> however, it often suffers from changes in sensitivity to scale, illumination, and viewpoint. It is also possible to use feature-based approaches (e.g. SIFT,<sup>7</sup> ASLFEAT<sup>8</sup>) which have been proposed for future missions such as the upcoming IM-1 lunar lander.<sup>2</sup> Databases of such

---

\*Graduate Student, Guggenheim School of Aerospace Engineering, Georgia Institute of Technology, Atlanta, GA 30364.

†Associate Professor, Guggenheim School of Aerospace Engineering, Georgia Institute of Technology, Atlanta, GA 30364.

features for small bodies (some of which have similar reflectance properties to the Moon) have also been created in recent years.<sup>9</sup> Many popular feature-based descriptors are scale-invariant and may be robust to changes in illumination and viewing conditions, however, matching performance will eventually degrade. In general, descriptors of a single feature created from two images of the same scene will not be the same if they are captured under significantly different illumination and viewing conditions. Alternatively, it is possible to perform matching using specific landmarks, though this comes with the disadvantage that landmarks may not be uniformly distributed across the surface of bodies. For example, since crater rims are well modeled by conics,<sup>10</sup> crater clusters may be used to compute quantities that are constant (invariant) under Euclidean and projective transformations.<sup>11–13</sup> It is not always possible to compute invariants, however, when it is, the number of distinct invariants may be enumerated. If they exist, invariants for a match are algebraic quantities that don't change when a given transformation is applied to the model. Simple models are often required for problems to be tractable (points, polynomials, and rational functions).<sup>14,15</sup>

Now, recall that classical feature-based methods describe the brightness pattern surrounding a feature without any direct knowledge of the underlying scene. The relationship between image brightness and surface reflectance can be determined.<sup>1</sup> Several lunar reflectance models exist and are in general functions of the illumination direction, the viewing direction, and the surface reflectance properties. With respect to surface reflectance parameters, models range from simple, diffuse Lambertian to the specialized Hapke model.<sup>16</sup> While the Hapke model provides a high-fidelity model of the Moon,<sup>17</sup> it is also developed empirically with tightly coupled surface reflectance parameters. For a spacecraft passing over the surface of a body, it is often the case that the illumination direction may be determined from an onboard sun sensor, and the viewing direction may be determined from a calibrated camera and a known attitude from other navigation sensors.

This work develops a reduced-order lunar reflectance model for illumination-informed TRN. We examine which parameters contribute the most to lunar reflectance while considering the differences in reflectance properties from different lunar landforms (e.g. maria, highlands). The lack of observability for parameters in the Hapke model is demonstrated, and this information is used to construct a simplified model. Finally, the construction of a surrogate model for analysis using invariant theory is discussed.

## IMAGING THE MOON

### Scene Appearance in Lunar Images

The appearance of a terrain patch depends on how much light is reflected from the surface and reaches the viewer. On bodies without an atmosphere (e.g., the Moon), reflectance is primarily controlled by the surface reflectance properties and the reflectance geometry (illumination, viewing, and surface normal directions).<sup>16</sup> Without the atmospheric scattering of light, shadows appear particularly harsh and their appearance is driven by illumination geometry. Specifically, on the Moon, scene appearance is known to be a function of phase angle (between the incidence and emission directions, see Fig. 3).<sup>2,16</sup>

Apollo 15 metric camera images of a crater cluster in Mare Imbrium are shown in the first row of Figure 1 and illustrate the expected increase in scene brightness with decreasing phase angle (left to right). The crater cluster's position and orientation change slightly as the images are captured over multiple orbits and the labels in each image mark corresponding craters between images. The camera is pointed nadir in all three images, and therefore, the decrease in phase angle from left

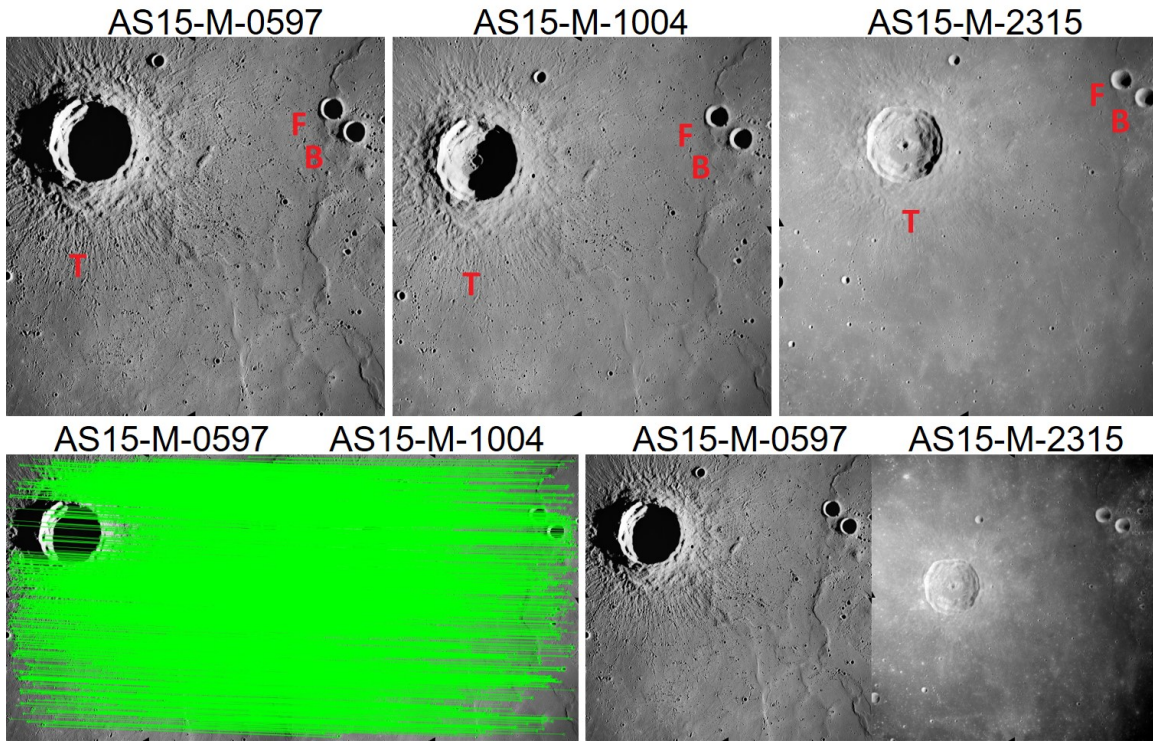


**Figure 1. The appearance of landforms within lunar maria changes drastically with decreasing phase angle (top row; left to right) such that feature matching performance (ASLFeat) degrades as the difference in phase angle increases between two images (bottom row; left to right). Apollo 15 metric camera images courtesy of NASA/JSC/ASU.**

to right is largely due to changes in illumination direction over multiple orbits. In all three images, most surface features are primarily discernible from the shadows cast over the surface. The shadows cast from surface features are most visible in the leftmost image when the phase angle is largest (i.e. the Sun is lowest on the horizon). As the Sun rises in the sky (center image), many features become less pronounced until they are washed out and not easily recognizable (right image). Now, we (humans) are still able to recognize that the images in each figure are of the same terrain patch by matching landmarks in each image. However, this may be difficult for computer vision algorithms, specifically feature descriptors, which rely on the local brightness patterns in each image to perform matching. Descriptors of a single feature from two images of the same scene will not be the same if they are captured under significantly different illumination and viewing conditions

The decrease in matching performance expected under significant illumination changes is shown in the second row of Figure 1. Matches are made between two image pairs from the set of three using the ASLFeat<sup>8</sup> feature descriptor, followed by an outlier rejection process. The left image is compared to the center and right images with the change in phase angle being larger in the second image comparison (left-right images). The first image pair comparison in Figure 1 produced 4700 matches while no matches were found in the second image pair. A similar result is shown in Figure 2 using images of the transition from mare to lunar highlands near Taurus-Littrow Valley. The first image pair produced 604 matches and again zero in the second image pair.

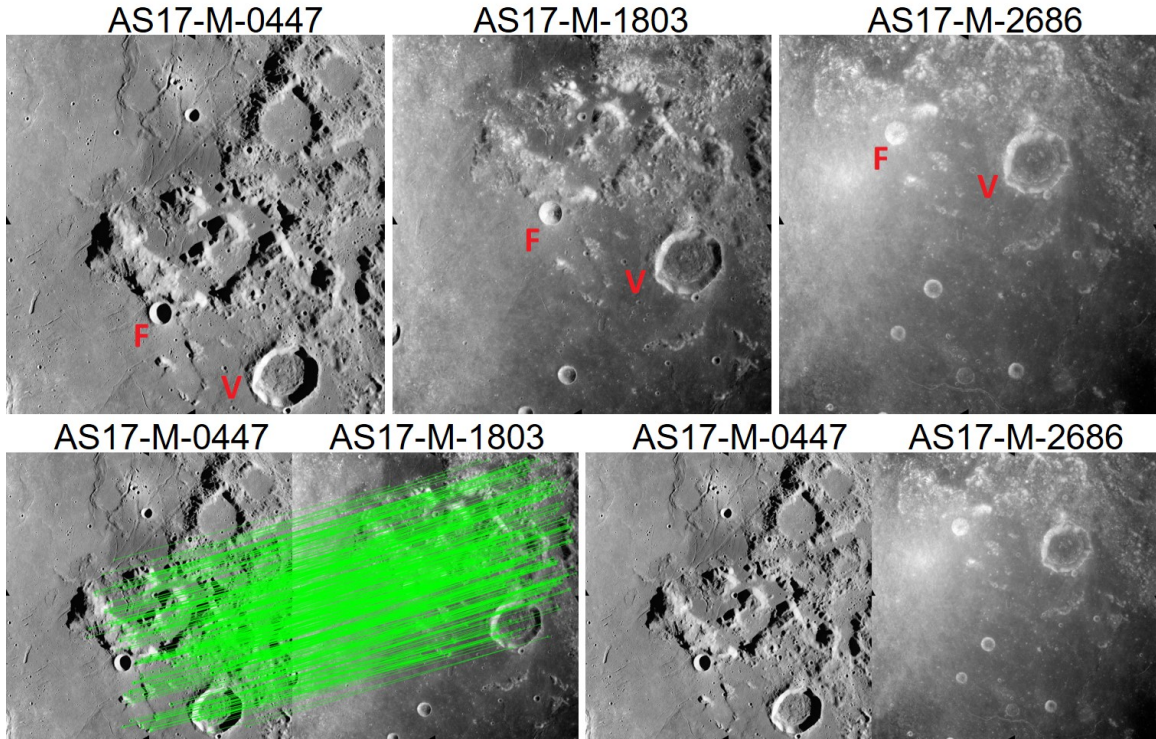


**Figure 2. The appearance of the lunar highlands changes drastically with decreasing phase angle (top row; left to right) such that feature matching performance (ASLFeat) degrades as the difference in phase angle increases between two images (bottom row; left to right). Apollo 17 metric camera images courtesy of NASA/JSC/ASU.**

## Reflectance Modeling and Geometry

Consider light falling on an arbitrary terrain patch of the lunar surface with irradiance  $J$  (power per unit area). On the lunar surface, the Sun is the dominant light source and subtends a small area of the extraterrestrial sky. Therefore, we consider the Sun as a point source and the irradiance can be written as the magnitude of the irradiance and a unit vector (incidence direction). From the patch of terrain to the Sun we have,  $\mathbf{J} = J\hat{s}$ , as shown in Figure 3. The light interacts with the surface and is reflected into *many* directions with radiance  $I$  (power per unit foreshortened area per unit steradian). Now, say a spacecraft passing overhead is equipped with a camera such that the radiance leaving the surface toward the camera can be expressed with the emission unit vector  $\mathbf{I} = I\hat{e}$ . There are multiple parameterizations for the illumination and viewing geometry, however, it's quite common to use a surface unit normal vector  $\hat{n}$  to define inter-vector angles,  $i$ , and  $e$ , between their respective incidence and emission directions. A third angle, the phase angle, is formed directly between the incidence and emission vectors.

There are multiple types of reflectance,<sup>16,18,19</sup> however, we will only consider bi-directional reflectance (also called directional-directional). The first adjective refers to the collimation of the incoming light and the second to the type of detector. A bi-directional reflectance function is valid given 1) the assumption of a point illumination source delivering collimated light to the surface, 2) the lack of atmosphere to diffuse light, and 3) the use of a directional detector (the camera). Note that light scattering is a linear process regardless of the type of reflection.<sup>16</sup> Therefore, if we con-

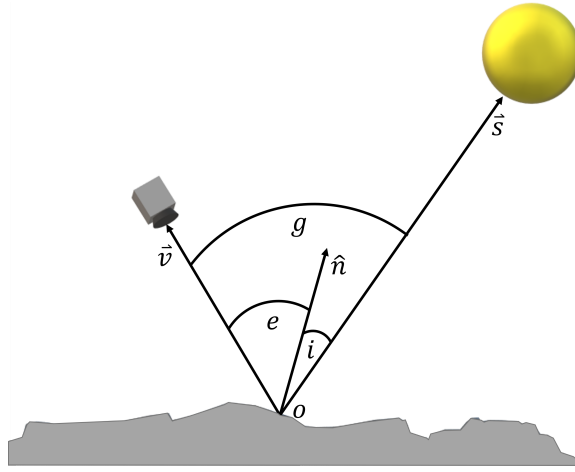


**Figure 3.** The reflectance geometry for an arbitrary point,  $o$ , is defined from vectors for the surface normal,  $\hat{n}$ , the illumination source,  $\vec{s}$ , and the observer,  $\vec{v}$ . In general, the three vectors are not co-planar as depicted above.

sider the irradiance from the Sun as our input, and the radiance reflected toward the onboard camera as our output, we have a general expression for our model, a bi-directional reflectance distribution function (BRDF),

$$r(i, e, g) = I/J \quad (1)$$

as a function of the inter-vector angles. All the reflectance models discussed will follow this form.

### Lunar Surface Reflectance

Many BDRFs are empirical, however, only a few may be derived analytically. The Lambertian model, known since the 1700s,<sup>20</sup> is the simplest usable model and is based on the empirical observation that for some surfaces, the light reflected from a surface appears equally bright in all directions. No surface is perfectly Lambertian, however, it describes a diffuse surface well as

$$r_L(i) = \frac{K_L}{\pi} \cos(i) \quad (2)$$

which is only a function of the incidence angle,  $i$ , and the Lambertian albedo  $K_L$ . It is useful for high-albedo, matte surfaces where a substantial percentage of the incoming light is reflected off the body. In addition, it has been shown that no invariants exist for a Lambertian surface imaged under arbitrary lighting and viewing conditions.<sup>21</sup>

Slightly more complicated is the Lommel-Seeliger model, which is amongst the simplest reflectance models that can be derived from first principles.<sup>22</sup> This model incorporates a dependence on emission angle and is the most complex model which can be described analytically. The surface reflectance for the Lommel-Seeliger model is

$$r_{LS}(i, e) = \frac{w}{4\pi} \frac{\cos(i)}{\cos(i) + \cos(e)} \quad (3)$$

where  $w$  is the single scatter albedo. The model is useful for low-albedo planetary bodies with no atmosphere, such as the Moon and asteroids. The basic model does not consider the opposition

effect, however, it can be modified to do so.<sup>16</sup> The McEwen model<sup>23</sup> is called a lunar-like model and is a weighted combination of the Lambertian and Lommel-Seeliger model and given as

$$r_{LL}(i, e, g) = B_0(g) \left[ 2L(g) \left( \frac{\cos(i)}{\cos(i) + \cos(e)} \right) + (1 - L(g))\cos(i) \right] \quad (4)$$

where  $B_0$  is the surface albedo. The term  $L$  gives the percent contribution from the lunar-like component as

$$L(g) = \frac{Af(g)}{Af(g) + 2B} \quad (5)$$

where  $A$  and  $B$  are selected constants, and  $f(g)$  describes the angular distribution of light as a single particle phase function. In this form, the contribution from each model can be quantified and a single albedo term,  $B_0(g)$  can be defined which was not possible with earlier formulations. The Hapke model is an empirical model and it is the most complex BRDF with nine free parameters.<sup>16</sup> It's a popular model in planetary science applications because its many reflectance parameters all have direct connections to real surface properties. However, it can be difficult to analyze the importance of specific effects because all of them are highly coupled. It is built on the Lommel-Seeliger model and additional terms are included to account for high-order effects.<sup>16</sup> The model is given in a condensed form<sup>17</sup> as

$$r_H = \frac{wK}{4\pi} \frac{\cos(i)}{\cos(i) + \cos(e)} [p(g)(1 + B_{S0}B_S(g)) + M(i_e, e_e)][1 + B_{C0}B_C(g)]S(i, e, \psi) \quad (6)$$

with the Henyey-Greenstein phase function,  $p(g)$ , the coherent backscatter,  $B_S(g)$ , shadow hiding,  $B_S(g)$ , multiple scattering,  $M(i_e, e_e)$ , and shadowing function,  $S(i, e, \psi)$  given in the Appendix. The Hapke parameters are listed in Table 1.

**Table 1. The nine Hapke parameters.**

Parameter	Description
$w$	Single scattering albedo
$b$	Henyey-Greenstein double-lobed single particle phase function shape parameter
$c$	Henyey-Greenstein double-lobed single particle phase function relative strength parameter
$B_{C0}$	Amplitude of coherent backscatter opposition effect (CBOE)
$h_c$	Angular width of CBOE
$B_{S0}$	Amplitude of shadow hiding opposition effect (SHOE)
$h_s$	Angular width of SHOE
$\theta$	Effective value of photometric roughness
$\phi$	Filling factor

Determining the reflectance parameters for a given model is a challenging problem. For most bodies, regolith is not available for laboratory experiments, and even for the Moon, samples are limited to those returned from the Apollo landing sites. These sites included both mare and highlands, however, the Moon's surface is far from homogeneous. Fortunately, radiometric techniques have been developed to estimate the estimate parameters. A spatially resolved Hapke parameter map divided into  $1^\circ \times 1^\circ$  tiles has been created using a model fitting procedure with Lunar Reconnaissance Orbiter (LROC) Wide angle Camera (WAC) images.<sup>17</sup> Multiple images of the entire mapped surface were required under many illumination and viewing conditions so estimates are not biased to a given configuration. To avoid difficulties introduced by the highly coupled Hapke model parameters, only four parameters free parameters ( $w$ ,  $b$ ,  $B_{S0}$ ,  $h_S$ ) were allowed, two ( $c$ ,  $\bar{\theta}_p$ ) are

derived from other Hapke parameters, and the remaining three parameters ( $B_{C0}$ ,  $h_S$ ,  $K(\phi)$ ) were neglected. To be precise, shadow hiding strength,  $B_{S0}$  is only free within a  $\pm 3^\circ$  band about the equator and is derived outside of that region. The coherent backscatter opposition effect (CBOE) occurs at much smaller phase angles than the shadow hiding opposition effect (SHOE) and those parameters ( $B_{C0}$ ,  $h_C$ ) are assumed to be folded into the SHOE terms ( $B_{C0}$ ,  $h_C$ ). The porosity factor (a function of filling factor  $\phi$ ) is directly proportional to the single-scatter albedo,  $w$ , and is neglected to avoid coupling. The final product is a set of 7 parameter maps, one for each of the 7 wavelengths captured by the LROC WAC.

## HAPKE PARAMETER ANALYSIS

We utilize the spatially resolved Hapke parameters to determine which contributes the most significantly to scene appearance. First, the lunar Hapke parameters are shown to naturally cluster by large-scale landforms allowing regions with similar properties to be analyzed independently. We then show which parameters are highly correlated to determine which parameters contribute most uniquely to surface reflection. We examine the total reflectance for a set of models of increasing fidelity to determine how individual effects contribute to reflectance. Finally, we examine the observability of the Hapke parameters.

### Identifying Lunar Landforms

We can see the composition of the lunar surface is not homogeneous by inspection of the Moon with the naked eye. Inspection of the Clementine albedo mosaic<sup>24</sup> in Figure 4 further reveals three large-scale landforms: the maria, the highlands, and high-albedo crater ejecta regions within the highlands. Histograms of the spatially resolved Hapke parameters show three of the four parameters have multi-modal distributions. From these two observations, we expect that a single reduced-order model may not be sufficient for all terrain types.

Using the k-means clustering algorithm, we segment the Hapke parameter map using two, three, and four clusters ( $k = 2, 3, 4$ ) which are shown in the cluster maps in Figure 4. With  $k = 2$ , we see

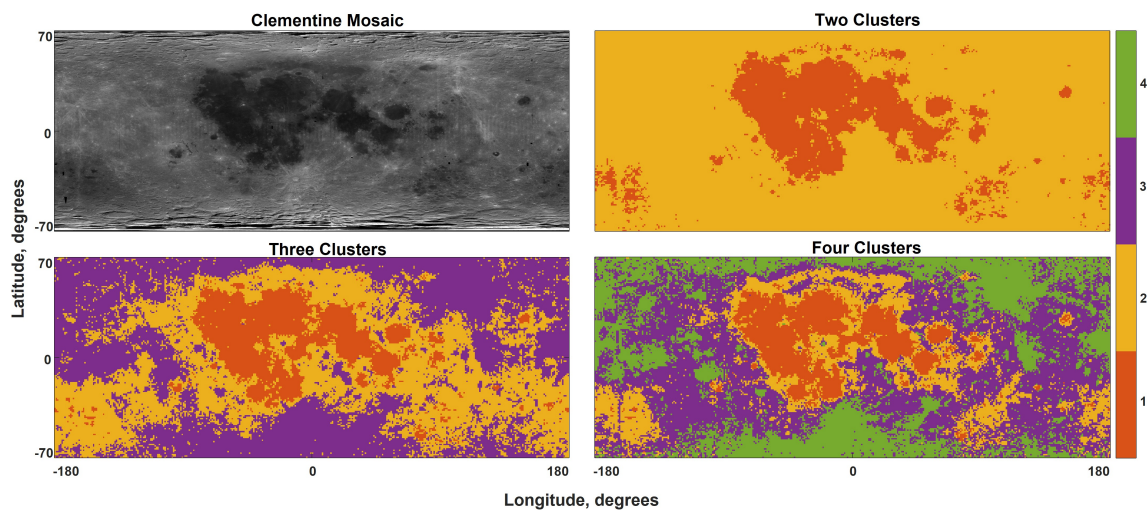


**Figure 4.** Clusters generated from resolved Hapke parameters are consistent with large-scale landforms (maria and highlands) depicted by the Clementine albedo mosaic.<sup>24</sup>

the two clusters formed are largely consistent with the lunar maria (orange) and highlands (yellow) visible in the Clementine data. Increasing to three clusters, we note that a cluster corresponding to the high-albedo region (purple) forms. Adding additional clusters ( $k \geq 4$ ) doesn't demonstrate a clear improvement in segmentation, and they appear to simply insert tiers between the lunar maria and the high-albedo clusters without segmenting new unique landforms. Therefore, we selected a three-segment cluster. This result enables a more pointed analysis from which we can determine if different lunar regions require different fidelity reflectance models.

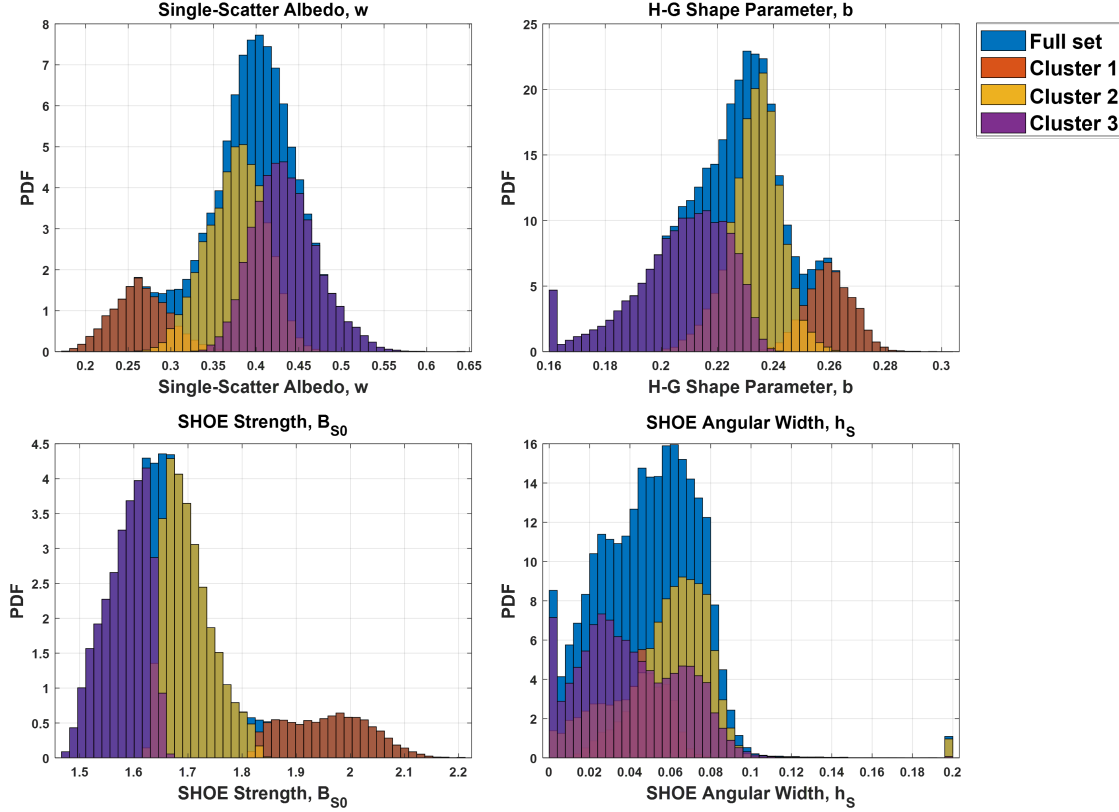


**Figure 5. The multi-modal Hapke parameter distributions can be decomposed into a three cluster segmentation consisting of maria, lunar highlands, and high-albedo crater ejecta**

### Parameter Correlation

Here, we examine correlations between each of the four independent parameters for each cluster and look for competing effects between parameters. The correlation matrices in Figure 6 show the correlation coefficients for each parameter pair decomposed by cluster. The terms are ordered to show dominant correlations. First, we note that the single-scatter albedo and H-G shape parameters are uncorrelated across all three clusters indicating each contributes independent effects to the reflection output. However, these parameters are correlated with the SHOE relative strength. The single-scatter albedo correlation decreases moving from maria (cluster 1) to ejecta (cluster 3) while the H-G correlation increases. Regardless, this is the first indication that the SHOE relative strength term can be eliminated or replaced by a functional dependence on single-scatter albedo and H-G shape parameters to simplify of the model. We note though that this is likely due to the functional

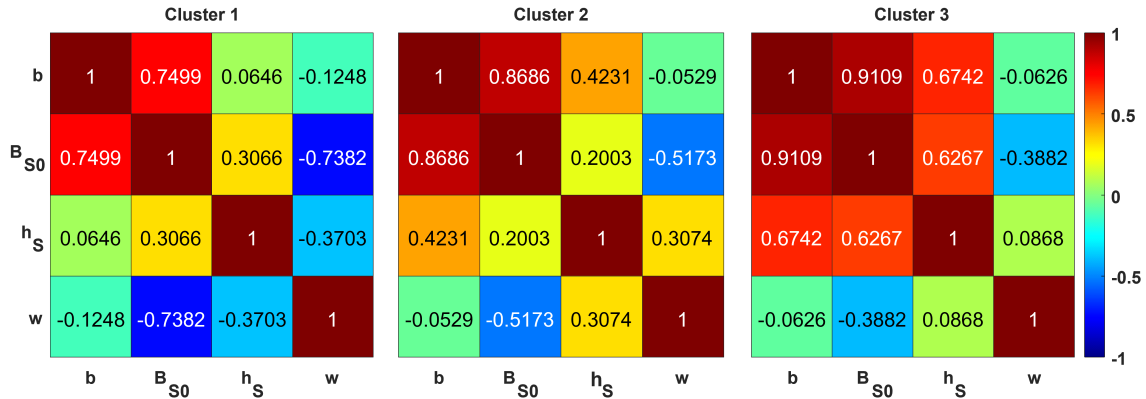


**Figure 6. Hapke parameter correlation matrices indicate single-scatter albedo ( $w$ ) and H-G shape parameter ( $b$ ) are consistently uncorrelated across clusters, however, both are fairly well correlated with SHOE strength ( $B_{S0}$ ).**

dependence of SHOE relative strength on these terms during the fitting process.<sup>17</sup> Finally, we note that the general correlation between terms increases moving from maria (cluster 1) to high-albedo crater ejecta (cluster 3). This correlation is likely because maria tend to be lower latitude features, and large correlations between parameters at high latitudes were previously attributed to a lack of low incidence and phase angle samples at these latitudes.<sup>17</sup> Still, from these results we assert that the single-scatter albedo and H-G shape parameter appear to contribute independent effects to the reflection while the correlations with the SHOE relative strength are redundant and the term may not be necessary for a TRN model.

### Reflectance Model Comparison

In this section we demonstrate that 1) each of the three clusters produces unimodal reflectance distributions for each model, 2) the maria clusters largely make up the lower reflectance modes while the two higher reflectance modes are largely split between the higher reflectance mode, and 3) contributions from multiple scattering and SHOE increase the reflectance, but photometric roughness negates those effects. From the available Hapke parameters, we generate reflectance model distributions for a Lambertian model plus a set of five reflectance models starting with the Lommel-Seeliger model and incrementally adding contributions from the H-G phase function, multiple scattering (IMSA), SHOE, and finally photometric roughness (which is the full Hapke model). When we decompose the bi-modal reflectance distributions by contribution from each cluster, we see that the maria cluster is largely responsible for the low reflectance mode while the other two highland clusters split the high reflectance mode (see Figure 7). More importantly, the reflectance distributions of each cluster remain ordered, and we see from inspection there are two main effects of increasing model complexity. The first is a right shift in each distribution and the second is the widening of the distribution range when multiple scattering and SHOE effects are introduced. These effects are also easily discernable in the Figure 8 box plots in Figure 8 from which we see that the contribution from SHOE is cluster dependent. The crater ejecta cluster has the greatest SHOE contribution followed by the general highlands cluster. Regardless, we see that the introduction of the photometric roughness term nearly negates the increase in reflectance from multiple-scattering (IMSA) and SHOE contributions. With respect to the final reflectance distributions, a two-parameter model consisting of single-scatter albedo and the H-G shape parameter approximates the Hapke model better than a

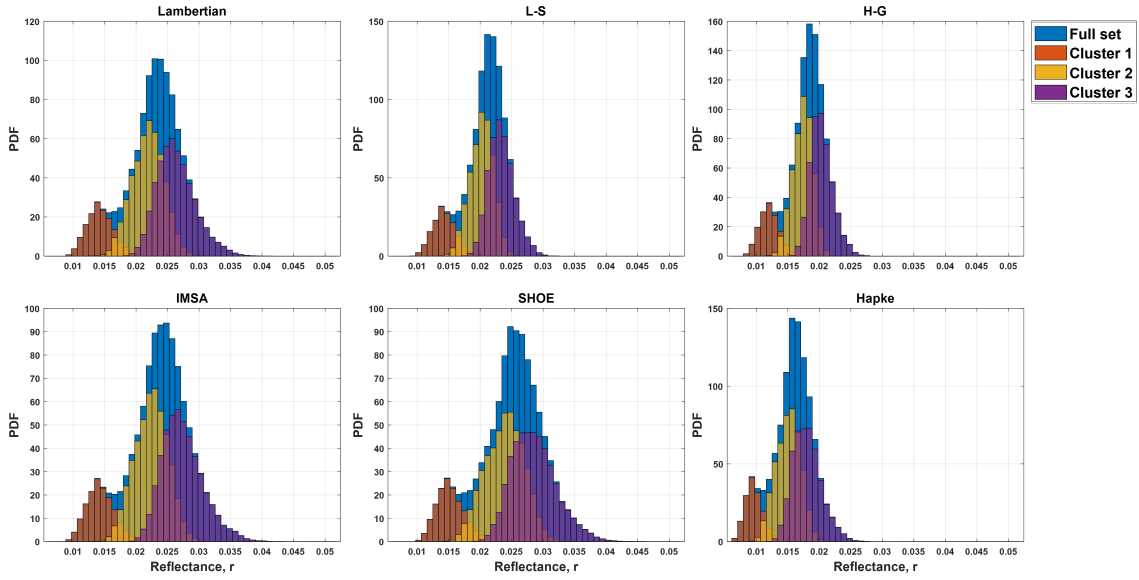


**Figure 7.** The distribution of reflectance from the Hapke model is more consistent with lower fidelity models (L-S and H-G) than higher fidelity models with multiple scattering and opposition effect.

model truncated after the higher order multiple-scattering (IMSA) or SHOE effects.

### Observability Analysis

In this section show that the independent parameters available are observable, but that SHOE relative strength is nearly unobservable. To estimate the observability of each Hapke parameter, we must compute the partial derivatives of the reflectance model with respect to each parameter. Given that only four parameters are available from the resolved Hapke parameter map, we consider the reduced reflectance model

$$r(i, e, g) = \frac{w}{4\pi} \frac{\cos(i)}{\cos(i) + \cos(e)} p(g)(1 + B_{S0}B_S(g)) \quad (7)$$

which only contains the single-scatter albedo, H-G phase function, and SHOE parameters.

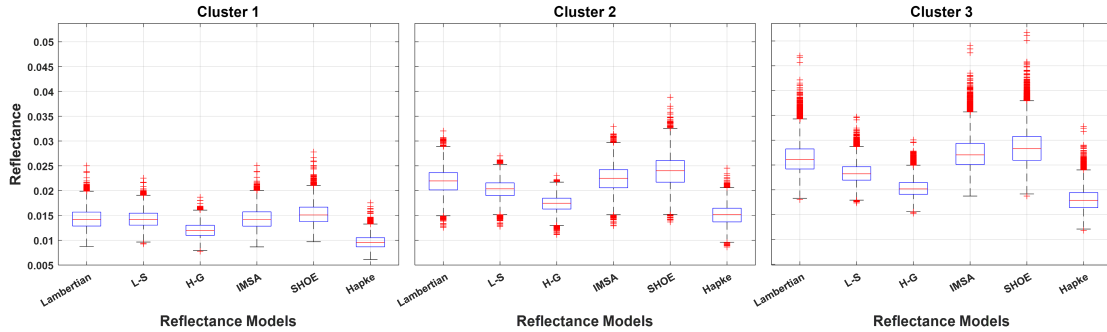


**Figure 8.** The box plot highlights that the increased reflectance from multiple-scattering (IMSA) and SHOE effects are effectively canceled by the inclusion of photometric roughness effects (Hapke) for each cluster.

To determine the observability of the parameters we compute the Gramian for the measurement matrix  $C$  as  $O = C^T C$ . The measurement matrix is constructed by stacking the partial derivatives evaluated at different viewing and illumination conditions with the Hapke parameters fixed at the median value of each cluster’s distribution. For this system to be observable, the Gramian must be a full rank (rank 4) matrix. In addition to a binary (observable or unobservable) result, we can determine the relative observability of each parameter from the eigenvalues,  $\lambda_i$ , of the Gramian.<sup>25</sup> We use an SVD approach in this work and take advantage of the fact that the singular values of  $C$  are positive square roots of the Gramian eigenvalues,  $s_i = +\sqrt{\lambda_i}$ . Larger singular values indicate eigenvector directions which are more observable.

The eigenvalues in Table 2 show that the system is fully observable for each cluster, however, the last eigenvector is much smaller than the others and is therefore much less observable. The eigenvectors for cluster 1 are also given and are representative of the 2nd and 3rd clusters’ eigenvalues. The eigenvector corresponding to the least observable eigenvalue,  $s_4$ , is almost completely aligned with the SHOE relative strength parameter. We note that the lack of observability for SHOE relative strength may be caused by its functional dependence on other parameters during the fitting process. Regardless of the cause, the lack of observability reduces the significance of the parameter in a reduced-order model.

**Table 2. The singular values and eigenvectors show the SHOE parameter,  $B_{S0}$ , is much less observable than the others.**

Singular Values	Clusters			Eigenvectors for $s_1$ (cluster 1)			
	1	2	3	$v_1$	$v_2$	$v_3$	$v_4$
$s_1$	23.8589	25.2496	26.4795	-0.6970	0.6436	-0.3159	-0.0120
$s_2$	5.9145	7.0224	7.2269	-0.3406	-0.6850	-0.6426	-0.0424
$s_3$	1.2286	1.2704	1.7416	-0.0207	-0.0202	-0.0335	0.9990
$s_4$	0.1325	0.1934	0.1911	-0.6306	-0.3407	0.6973	0.0034

## CONCLUSION

Matching features from one image to another (or to a map) is a challenging problem that is exacerbated by large changes in illumination. This work takes the first steps toward developing an illumination-informed feature descriptor for terrain relative navigation. We found the most significant parameters for the Hapke reflectance model are the single-scatter albedo and the H-G phase function shape parameter. We note that from the data available, only four of the nine Hapke parameters were evaluated. Since the landforms and lunar surface properties are not uniform, care was taken to evaluate the model for different landforms, though the final results indicate the same set of parameters is important for all landforms. As expected from a simple inspection of the Hapke model, many of the parameters are highly correlated with the exception of the single-scatter albedo and H-G phase function shape parameter. Of particular interest is the observation that photometric roughness effects cancel out contributions from multiple scattering and opposition effects. This indicates that for all its complexity, generating approximate models can be done with a two parameter system. Finally, an observability analysis showed that shadow hiding opposition effects were not observable. With this two parameter model, future work includes investigating formulations for potential surrogate functions which would be useful for invariant theory analysis.

## ACKNOWLEDGMENT

The work of C. De Vries was partially supported through a NASA Space Technology Graduate Research Opportunities (NSTGRO) Fellowship (80NSSC22K1185).

## REFERENCES

- [1] B. K. Horn, *Robot Vision*. The MIT Press, ISBN: 9780262081597, first ed., 1986.
- [2] J. A. Christian, L. Hong, P. McKee, R. Christensen, and T. P. Crain, “Image-Based Lunar Terrain Relative Navigation Without a Map: Measurements,” *Journal of Spacecraft and Rockets*, Vol. 58, 2021, pp. 164–181, 10.2514/1.A34875.
- [3] A. E. Johnson, A. R. Klumpp, J. B. Collier, and A. A. Wolf, “Lidar-based hazard avoidance for safe landing on Mars,” *Journal of Guidance, Control, and Dynamics*, Vol. 25, 2002, pp. 1091–1099, 10.2514/2.4988.
- [4] Y. Cheng, J. Goguen, A. Johnson, C. Leger, L. Matthies, M. S. Martin, and R. Wilson, “The Mars Exploration Rovers Descent Image Motion Estimation System,” *IEEE Intelligent Systems*, Vol. 19, 2004, pp. 13–21, 10.1109/MIS.2004.18.
- [5] A. E. Johnson, Y. Cheng, N. Trawny, J. F. Montgomery, S. Schroeder, J. Chang, D. Clouse, S. Aaron, and S. Mohan, “Implementation of a Map Relative Localization System for Planetary Landing,” *Journal of Guidance, Control, and Dynamics*, Vol. 46, No. 4, 2023, pp. 618–637, 10.2514/1.G006780.
- [6] R. D. Olds, C. J. Miller, C. D. Norman, C. E. Mario, K. Berry, E. Palmer, O. S. Barnouin, M. G. Daly, J. R. Weirich, J. A. Seabrook, C. A. Bennett, D. Lorenz, B. Rizk, B. J. Bos, and D. S. Lauretta, “The Use of Digital Terrain Models for Natural Feature Tracking at Asteroid Bennu,” *The Planetary Science Journal*, Vol. 3, 5 2022, p. 100, 10.3847/psj/ac5184.
- [7] D. G. Lowe, “Distinctive Image Features from Scale-Invariant Keypoints,” *International Journal of Computer Vision*, Vol. 60, 2004, pp. 91–110, 10.1023/B:VISI.0000029664.99615.94.
- [8] Z. Luo, L. Zhou, X. Bai, H. Chen, J. Zhang, Y. Yao, S. Li, T. Fang, and L. Quan, “ASLFeat: Learning Local Features of Accurate Shape and Localization,” *2020 IEEE/CVF Conference on Computer Vision and Pattern Recognition (CVPR)*, 2020, pp. 6588–6597, 10.1109/CVPR42600.2020.00662.
- [9] T. Driver, K. Skinner, M. Dor, and P. Tsiotras, “AstroVision: Towards Autonomous Feature Detection and Description for Missions to Small Bodies Using Deep Learning,” *Acta Astronautica*, Vol. 210, 2023, pp. 393–410, 10.1016/j.actaastro.2023.01.009.
- [10] J. A. Christian, H. Derksen, and R. Watkins, “Lunar Crater Identification in Digital Images,” *Journal of the Astronautical Sciences*, Vol. 68, 12 2021, pp. 1056–1144, 10.1007/s40295-021-00287-8.
- [11] J. A. Christian, “A Tutorial on Horizon-Based Optical Navigation and Attitude Determination with Space Imaging Systems,” *IEEE Access*, Vol. 9, 2021, pp. 19819–19853, 10.1109/ACCESS.2021.3051914.
- [12] Y. Cheng and A. Ansar, “Landmark Based Position Estimation for Pinpoint Landing on Mars,” *Proceedings of the 2005 IEEE International Conference on Robotics and Automation*, 2005, pp. 1573–1578, 10.1109/ROBOT.2005.1570338.
- [13] D. Forsyth, J. Mundy, A. Zisserman, C. Coelho, A. Heller, and C. Rothwell, “Invariant descriptors for 3D object recognition and pose,” *IEEE Transactions on Pattern Analysis and Machine Intelligence*, Vol. 13, No. 10, 1991, pp. 971–991, 10.1109/34.99233.
- [14] J. L. Mundy and A. Zisserman, *Introduction-towards a new framework for vision*, pp. 1–39. Cambridge, MA: MIT Press, 1991.
- [15] J. A. Christian and H. Derksen, “Invariant Theory as a Tool for Spacecraft Navigation,” AAS/AIAA Astrodynamics Specialist Conference, Charlotte, NC, 2022.
- [16] B. Hapke, *Theory of Reflectance and Emittance Spectroscopy*. Cambridge University Press, 1 2012, 10.1017/CBO9781139025683.
- [17] H. Sato, M. S. Robinson, B. Hapke, B. W. Denevi, and A. K. Boyd, “Resolved Hapke parameter maps of the Moon,” *Journal of Geophysical Research E: Planets*, Vol. 119, 2014, pp. 1775–1805, 10.1002/2013JE004580.
- [18] F. E. Nicodemus, “Reflectance Nomenclature and Directional Reflectance and Emissivity,” *Appl. Opt.*, Vol. 9, Jun 1970, pp. 1474–1475, 10.1364/AO.9.001474.
- [19] N. Nicodemus, “Geometrical considerations and nomenclature for reflectance,” *U. S. Department of Commerce, National Bureau of Standards*, 1997.
- [20] J. Lambert, *Photometria*. 1760.

- [21] H. F. Chen, P. N. Belhumeur, and D. W. Jacobs, “In search of illumination invariants,” Vol. 1, IEEE Computer Society, 2000, pp. 254–261, 10.1109/CVPR.2000.855827.
- [22] M. Fairbairn, “Planetary Photometry: The Lommel–Seeliger Law,” *Journal of the Royal Astronomical Society of Canada*, Vol. 99, 2005, pp. 92–93.
- [23] A. S. McEwen, “Exogenic and endogenic albedo and color patterns on Europa,” *Journal of Geophysical Research*, Vol. 91, 1986, p. 8077, 10.1029/jb091ib08p08077.
- [24] E. M. Eliason, “Clementine UVVIS Digital Image Model,” 1999, 10.17189/1520339.
- [25] S. L. Brunton and J. N. Kutz, *Data-Driven Science and Engineering*. Cambridge University Press, 1 2019, 10.1017/9781108380690.